Asymmetric 3D elastic-plastic strain-modulated electron energy structure in monolayer graphene by laser shocking

Maithilee Motlag[1], Prashant Kumar[1,2,3], Kevin Y. Hu[1,2,4], Shengyu Jin[1,2], Ji Li[1,2], Jiayi Shao[2], Xuan Yi[2,6], Y. H. Lin[7,10], J. C. Walrath[7], Lei Tong[9], Xinyu Huang[9], R. S. Goldman[8*], Lei Ye[9*], Gary J. Cheng[1,2,5*]

1. School of Industrial Engineering, Purdue University, West Lafayette, Indiana, USA-47907.
2. Birck Nanotechnology Centre, Purdue University, West Lafayette, Indiana, USA-47907.
3. Department of Physics, Indian Institute of Technology Patna, Bihta Campus, Bihar 801106, INDIA.
4. University at Buffalo—SUNY, 3435 Main Street, Buffalo, NY 14214, USA.
5. School of Mechanical Engineering, Purdue University, West Lafayette, Indiana, USA-47907.
6. School of Electrical and Computer Engineering, Purdue University, West Lafayette, Indiana, USA-47907.
7. Department of Physics, University of Michigan, Ann Arbor, MI, USA-48109
8. Department of Materials Science and Engineering, University of Michigan, Ann Arbor, MI, USA-48109.
9. School of Optical and Electronic Information, Huazhong University of Sci. and Tech., Wuhan, 430074, China
10. current address: Department of Physics, University of Maryland, College Park, MD 20742

*Correspondence: Gary J. Cheng, Phone: +1 765 49-45436, e-mail: gjcheng@purdue.edu; R. S. Goldman, Phone: +1 734 647-6821, email: rsgold@umich.edu; Lei Ye, Phone: +86 27- 87792461, email: leiye@hust.edu.cn

Abstract:

Graphene has a great potential to replace silicon in prospective semiconductor industries due to its outstanding electronic and transport properties; nonetheless, its lack of energy band gap is a substantial limitation for practical applications. Therefore, precise electronic band gap tuning in graphene is a critical challenge to facilitate its developments in electronic, photonic, and

optoelectronic applications**. To date, straining graphene to break its lattice symmetry is perhaps the most efficient approach towards realizing band gap tunability in graphene. However, due to the weak lattice deformation induced by uniaxial or in-plane shear strain, most strained graphene studies have yielded band gaps < 1 eV. In this work, we report a modulated inhomogeneous local asymmetric elastic-plastic straining that utilizes GPa-level laser shocking at a high strain rate ($d\varepsilon/dt$) ~ 10^{6-7} /s, with excellent formability, inducing tunable band gaps in graphene of up to 2.1 eV, as determined by tunneling spectroscopy. The work function tunability of graphene is also realized by this approach, which is demonstrated by KPFM (Kelvin probe force microscope) to facilitate the alignment of energy levels in graphene-semiconductor heterojunctions which can be used to eliminate energy barriers in heterostructured electronic or optoelectronic devices. High-resolution imaging and Raman spectroscopy reveal strain-induced modifications to the atomic and electronic structure in graphene and first principles simulations predict the measured band gap openings. Thus, laser shock inhomogeneous asymmetric nano straining of graphene is an ultrafast, ambient technique which can be used for many other 2D crystals and their combinations. Laser shock modulation of semi-metallic graphene to a semiconducting material with controllable band gap is the first report of its kind, which has the potential to the electronic and optoelectronic industries.**

Keywords: Optomechanical 3D straining, Single layer graphene, Band gap engineering

Graphene, which consists of a two dimensional (2D) atomic sheet of sp^2 hybridized carbon, is one of the most significant materials for future applications[1-18] due to its extremely high electronic mobility, quantum Hall effect, high thermal conductivity, flexibility, optical transparency, molecular anchoring capability and superior mechanical strength. However, many electronic and optical characters are also in close relationship with finite bandgap for semiconductors, the lack of an energy band gap in graphene hinders the realization of high-performance field-effect transistors and optoelectronic devices[4, 19-27]. Moreover, modulation of the Fermi-level of graphene over a large range is also very difficult to circumvent heterojunction energy barriers, thus further limiting the development of graphene-based electronic or optoelectronic devices. Although extrinsic approaches[19-21] to open the band gap and modulate the work function of graphene have been attempted, including doping[22-23], hydrogen adsorption[24], formation of graphene nanostructures[25-26] and multilayers, they have not yet been able to tune work function and yielded large band gaps (always <1 eV)[27], as a result, the device performance based on graphene is still under restriction. Hence, an alternative method to modulate the electron energy structure of graphene is required to fully realize the potential of graphene in future semiconductor industry. To improve this intrinsic insufficiency of graphene,

strain-engineering is an effective method to achieve band gap opening. Based on the lattice symmetry of the wave vector at *K* point in graphene,[27, 28] it has been suggested that uniaxial tensile or compressive strain perpendicular or parallel to the C-C bonds would break the lattice symmetry, thus opening a band gap and changing the work function in graphene.[29-32] However, most strain-engineering work has only realized a small band gap opening, without effective nanoscale band gap control. To date, shear strain across bilayer graphene has been used to open the band gap to 0.3-0.4 eV[33]. Based on first principles calculations, Gui et. al. and Hicks et. al.[34-36], have proposed that the simultaneous expansions of C-C rings in two perpendicular directions can result in a pseudo gap of 0.48 eV. Ariza et. al.[37] have predicted that plastic deformation induced by the pentagonal and heptagonal rings associated with stacking faults and partial dislocations in graphene sheets would lead to significant band gap opening of 0.8 eV. Moreover, it has been reported that the simultaneous strain and curvature in graphene would locally alter the energy band structure[38-40], presumably leading to band gaps exceeding 1 eV. Here, an opto-mechanical approach has been studied to achieve asymmetric inhomogeneous elastic-plastic strain in monolayer graphene to modulate its band gap structure and Femi-level, realizing band gap development over 1.7~2.1 eV and a Femi-level range of 0.6 eV, for the first time.

In this work, a high strain rate ($d\varepsilon/dt$) ~ 10^6/s is performed by laser shock imprinting, which leads to excellent formability and toughening of graphene[41, 42], to realize inhomogeneous local asymmetric elastic-plastic strain in graphene. The strain is controllable by changing the incident laser power. Single-layer graphene was deformed via laser shocking onto an e-beam fabricated SiO_2 nanomold with designed geometries to open its band gap, whose dimensions can precisely be controlled, resulting in patterned strain profile over large areas. In addition, the KPFM results of strained graphene showed that the work function is controllable with range to ~0.6 eV, which is enough for energy barrier self-alignment in graphene-semiconductors based electronic and optoelectronic devices to achieve exciting performances. Scanning electron microscopy and atomic force microscopy were employed to characterize the deformed surface profile. Scanning tunneling spectroscopy was employed to evaluate the electronic band gap of single-layer inhomogeneous straining graphene. The atomic-scale strains in the graphene were quantified using high-resolution TEM, and subsequently used as input into molecular dynamics (MD) simulations. Density functional theory was used to perform band structure calculations. The large asymmetric plastic-elastic strain produced in graphene by laser shocking induced large graphene electronic band gaps while also permitting tuning of other important characteristics such as the graphene work function. The tunable inhomogeneous straining by laser shock is highly promising for material engineering, electronic and optoelectronic applications [43-46].

The experimental setup schematic is depicted in **Fig. 1(a)**. Graphene sheet is placed between the Si/SiO_2 mold and an aluminum film. The laser shock is performed on aluminum film and large strain is transduced to graphene layer. Several tens of GPa pressure shock are generated by tuning the laser power, thereby inducing 3D inhomogeneous strain in single-layer graphene; a small-scale MD simulation of strained monolayer graphene achieved by laser shock is shown in the inset. **Fig. 1(b)** shows the evolution of nanoshaped graphene. An animation of the simulation process of producing strained monolayer graphene is depicted in Supplementary Materials video 1. Nanotrenches with controlled dimensions (width and depth) were fabricated on SiO_2 substrates by electron beam lithography and then used as a mold for laser shock nanoimprinting. **Fig. 1(c)** and **1(d)** depict typical molds with varying trench widths all on one substrate. More detailed scales of nanotrench molds are shown in **Fig. 1(e)** and **1(f)**. Atomic force microscopic images of nanostrained laser shock nanoimprinted graphene are shown in **Fig. 1(g)** and enlarged **Fig. 1(h)** images of the graphene having the same width of 400 nm and depth of 100 nm corresponding with the mold shape, illustrating that the smooth curvature of shaped atomic graphene atomic structure can precisely be defined by the mold dimension and the laser shock pressure. We have also measured Raman spectra of graphene after laser shocking, at eight selected point's locations of nanotrench and another location between the nanotrenches (Fig. S1). Their corresponding Raman spectra mapping is shown in Fig. 1(i). In our experiments, the laser shock is directly performed on an aluminum foil to induce large strain which is transferred to graphene, so laser induced defects in graphene can be ignored. The high-quality graphene and clean transfer method can also eliminate the influence of contaminations on Raman peak shits. As a result, the Raman peak shifts can be attributed to the large strain in graphene. After laser shocking, the 2D peak (~2680 cm-1) and G peak (~1600 cm-1) both show obvious red shift from points b to h, indicating that the strain is largest at the trench edge, and then decreases from the trench edge to the center of the trench. To evaluate the crystal quality of graphene after laser shocking, the intensity ratio between D peak (~1350 cm^{-1}) and G peak (I_D/I_G) is also calculated (Fig. S1). The ratios are smaller than 0.7, and the ratio is largest at the trench edge with largest strain. From the edge to the center of the trench, the ratios show a declining trend, with a minimum value close to that of unstrained CVD monolayer graphene, which is in accordance with the strain distribution on graphene after laser shock.

The schematic diagram of the shaping of graphene is shown in **Fig. 2(a)**. STM based spectroscopy was carried out to evaluate the actual local band gaps in the strained graphene sheet to validate our assumption that the local inhomogeneous strains caused by laser shock resulted in the opening of the band gap of graphene. The local lattice strain profile as a function of position was calculated with help of molecular dynamics simulations to demonstrate the induced strain in graphene along the trench.

The calculated strain profile is depicted in **Fig. 2(b)** with largest strain located at the edge of the nanotrench. We also used variable separation scanning tunneling spectroscopy (VS-STM) to examine the influence of the inhomogeneous local strain on the local electronic structure of the strained graphene sheet. We have selected 7 points located at the curved graphene, as marked in Fig. 2(b). Point 1 is far away from the nano-trench, showing no strain at this point. The normalized differential conductance *(dI/dV)-V* is proportional to the surface density of states in graphene providing an estimate of the local effective band gap. The normalized differential conductance *(dI/dV)-V* as a function of bias voltage is depicted in **Fig 2(c)** at designated locations as shown in Fig. 2(b) which confirms the opening of the electronic band gap in strained graphene. For the unstrained graphene above the trench (point 1), the linear steep slope indicates that this location is metallic suggesting that the band gap is close to zero. However, at the edge of the trench (point 2), the negligible conductance in a large bias voltage region indicates a large strain induced band gap opening. The band gap opening decreases when the induced strain decreases at the respective position on the slope of the trench. **Fig. 2(d)** depicts the STM figure of the strained graphene across the same nanotrench (with dimensions of 400 nm width and 100 nm depth). To better illustrate the bandgap opening of graphene, we have selected 10 points along the same trench, and **Fig. 2(e)** shows the corresponding effective band gaps as a function of distance (nm) across the trench as shown by the dashed white horizontal line in Fig. 2(d). The *dI/dV* curves for selected points in Fig. 2(e) are included in the Supplementary Materials (Fig. S2). The highest effective band gaps of 1.3 ± 0.38 eV and 1.7 ± 0.24 eV are observed at the edge of the trench marked with the vertical dashed line whereas smaller band gap openings ranging from 0.55 ± 0.14 eV and 1.15 ± 0.14 eV are observed in the interior region of the trench. Thus, we observed the opening of the band gap of graphene up to 1.7 eV by straining in one step solely using laser shock produced large strains. The reason for the opening of the band gap at the trench can be attributed to combined elastic and plastic strains, which will be discussed later. Recent studies about strain-induced graphene suggest that the band gap opening is contributed from elastic in-plane straining [38-40]. On the other hand, this plastic-elastic strain can also tune Fermi level of graphene, leading to the elimination of energy barrier caused by misalignment of Fermi level in graphene-semiconductor heterojunction. **Fig. 2(g)** shows the topology image of laser shock imprinted graphene sample on Si/SiO_2 mold, where the sample surface is uniformly and periodically imprinted. **Fig. 2(f)** shows the CPD along the sample surface, ranging from 0.732 V to 0.643 V. Profile of the graphene sample and its corresponding KPFM is measured as shown in **Fig. 2(h).** Based on density functional theory calculation (DFT) of the work functions of the plastic-elastic strained graphene, the work functions of graphene at seven locations from the edge of the trench to the center (point A to G) is observed to increase substantially with increase of strain, as shown in **Fig. 2(i).** The work function

at the edge location of the trench with the largest strain was found to be a maximum (4.82 eV) and the work function at center was found to be a minimum (4.40 eV) from theoretical calculations. The measured work functions of the strained graphene trench at the corresponding seven locations in Fig. 2(b) are found to be the range of 4.39 eV-4.91 eV, which are obtained by subtracting the CPD from the work function of the tip. Due to the measured work function results, the tunable Fermi level of graphene can be up to ~0.6 eV, providing an important energy barrier self-alignment capability to achieve high performance for graphene-semiconductor devices.

Laser shock on another mold (Mold 2) with 300 nm width and 100 nm depth was also carried out. The effective band gap as a function of distance for Mold 2 is illustrated in Fig. S3 in the Supplementary Materials. When we compared the results for two different molds (Mold 1 and Mold 2), we observed a striking difference between band gap plots, which implies that the edge region has band gap opening as high as 2.1±0.25 eV in mold 2 case. The central regions exhibit a small band gap of 0.4 eV in the case of mold 1, whereas the band gap is as high as 1.0 eV in the central region for the mold 2 case. This is due to larger strain in mold 2 with narrower width, which suggests that laser shock imprinting technique can modulate the levels of strain in graphene by substrate design to precisely tune its band gap. **Fig. 3(a)** displays the large scale STM mapping of laser shock induced patterned graphene. The inset shows the fast Fourier transform (FFT) results for the graphene pattern, the periodicity of the signal indicates that the prominent band gap opening coincides with the pattern and no break in larger scale graphene is induced by laser shock. **Fig. 3(b)** shows the SEM image of the patterned graphene. **Fig. 3(c)-(i)** illustrate the STM measured *I-V* curves at several locations along the yellow line on Fig. 3(a). With the laser shock induced strain decreasing, the *I-V* curve steepens, and when the strain increases, the *I-V* curve becomes flatter, indicating the periodic modulation of band gap opening in graphene.

Fig. 4(a) is a high-resolution TEM image of the single layer graphene strained by mold 1. A close-up view of the marked region is presented in **Fig. 4(b)**, revealing aligned carbon atoms along three directions (orange arrows). Yellow hexagons marking carbon rings with alternate atoms are illustrated in **Fig. 4(c)**. To evaluate the uniformity in the structure of graphene, the blue triangle is depicted in Fig. 4(e), in which three blue edges are identical with the orange arrows in Fig. 4(b). **Fig. 4(d)** shows another region with a larger visible graphene structure**.** The close-up view of a marked region of **Fig. 4(d)** is shown in **Fig. 4(e)** along with the strain assessment measured by atomic distances. It is observed that atoms in two directions are relatively closer than the equilibrium distances in graphene as well as atomic distances in the third direction are larger, indicating non-uniform straining of graphene. We have also observed tension in one direction and compression in

other direction, inducing shear strain and bond angles changes in graphene structure. The atomic distances from TEM images were used to assess strain and to validate the molecular dynamics simulation results. Omicron (UHV) STM system was used to obtain the atomic resolved topographic image (I=10 nA, V=0.2Volt) and study the effect of laser shock straining on the atomic movements and reconfigurations. The STM images of graphene at three different locations along the trench which experienced different levels of straining are shown in **Fig. 4(f)-(h)**. In Fig. 4(f) near the trench valley, the hexagonal structure of graphene is preserved with only small distortion caused by atomic displacements, due to smallest strain in this area. However, at another location on the slope of trench (Fig. 4(g)), higher distortion in the hexagonal structure as compared to Fig. 4(f) can be observed, indicating higher levels of elastic strain in laser shocked graphene. At the trench edge location with the largest strain (Fig. 4(h)), few Stone-Wales defects are observed to indicate the occurrence of plastic deformations. Such reconfigurations occur in atomic sheets to release the strain in the systems. High resolution TEM cross sectional view (Fig. S4) was added to study the straining effects from the lattice parameters in the laser shock strained graphene on a 300nm width trench mold. The pixel intensity profile (Fig. S4(a)) was used to calculate the lattice distance between neighboring atoms. The elastic lattice strain can be estimated by calculating the distance between second neighboring carbon atoms compared to that of the unstrained lattice parameters (0.243nm) at six locations (Fig. S4(c)). The points of higher strains indicated plastic deformations i.e. presence of Stone-Wales defects and the reference distances for second neighboring carbon atom distances for such 5-7-7-5 membered rings were taken from the simulation as depicted in Fig. S4(d). The strains at various positions was summarized in Fig. S4(b). Thus, we conclude that laser shock can result in designed strain profile in graphene sheet leading to extreme levels of straining which generate plastic strain-induced atomic reconfigurations in graphene such as Stone-Wales defect formation and vacancy formations. Based on the HRTEM, we have also observed distinct deformations in inhomogeneous straining multilayer graphene induced by laser shock, as shown in Fig. S5. Even though the multilayer sample may not be as technically promising as single layer graphene, its ease of handling in practical devices makes it worth evaluating. In some designs the plastic strain induced at the edge of the trench is not desirable in graphene, since it creates huge distortions as compared to the unstrained graphene; however, it is acceptable under a tolerable level such that it would not disturb the atomic skeleton of graphene. To further prove the large band gap opening in laser shock is also applicable to mechanical exfoliated graphene sample, we also measured photoluminescence (PL) spectrum of inhomogeneous straining graphene. From the results (Fig. S6), the peak near 675 nm is PL response from Au substrate, which exists in all measured results. The PL result of graphene at the edge (point 1) presents a distinct broad peak with the end at 800 nm, indicating the large band gap opening due to the large elasto-

plastic strain. With the decrease of strain from the edge to the center (point 2 to 4), the reduction of PL intensity which is related with band gap of graphene is observed, suggesting the reduction of band gap opening with the decrease of laser shocking induced strain. The strong PL signal suggests that strained monolayer graphene possesses high quality. Thus, it would retain mobility which is perhaps the most significant attribute of graphene useful for fast nanoelectronics applications such as in FETs, sensing, THz wave guiding etc.

For strained graphene, the crystal structure is observed to be skewed hexagonal shape, which is influenced by both axial and shear strain components. The bond angles of carbon atoms in graphene are also observed to be different than 120˚, these results confirm asymmetric levels of inhomogeneous straining in graphene at the atomic scale. Since the enhanced level of strain differences in different directions would cause enormous asymmetries in the system, the dislocations in graphene would break the local symmetry thereby causing local rise of potential energy. We have closely followed experimental results on band gap opening with molecular dynamics simulations of laser shock straining of graphene and then estimated band gap employing DFT methods. It was not feasible to conduct simulations for the scale of the actual trench dimensions due to the enormous time and memory limitations; however, we kept the simulated depth-to-diameter ratio same as the real cases. Simulations were carried out on three different configurations to study the effect of the aspect ratio on straining and the band gap opening of graphene. Further details of the molecular dynamics and DFT simulations are explained in Supplementary Materials. To better validate the hypothesis that the band gap opening was due to localized dislocation-induced plasticity and asymmetric elasticity, we have focused on the stress strains at three locations, namely A, D and G, located at the edge of trench, slope of trench and center of trench, respectively. Permanent deformation was observed only at the edge for all three configurations which confirms that plasticity is observed only at the corner of strained graphene. Continuum crystal plasticity defines displacement field at every material point as against to atomistic description where we only have discrete atomic positions. Thus, to define a gradient, the displacement field is linearly interpolated between the atoms[47]. Stukowski and A. Arsenlis[48] developed a technique of separation of elastic and plastic decomposition of the deformation applied in molecular dynamics. With this technique, the bond vectors are mapped to the neighboring atoms to derive a stress-released state to measure atomic strains. More details of strain calculations are discussed in Supplementary Materials.

The mechanical responses of the strained graphene and the atomic lattices for the configuration with depth-to-diameter ratio of 100 nm/400 nm are studied as depicted in **Fig. 5**. Since Stone Wale's 5-7-7-5 defects in graphene is an evidence of plastic straining, the elasto-plastic stress-strain

response is observed only at location A (edge of nanotrench), as seen in **Fig. 5(a)**, where graphene sustains largest strain. The plastic regime is found beyond strains of 0.18 for this configuration. The atomic model of the deformed configuration at location A is depicted in **Fig. 5(b)**. Ratios of the bond lengths detected from simulations to the bond length of pristine graphene were calculated and plotted as seen in Fig. 5(b), where green marks average bond length of 1.42 Å. Onset of plasticity is marked by Stone Wall's 5-7-7-5 defects which are observed in Fig. 5(b). Extreme ratios are observed around plastically deformed 5-7-7-5 defects, leading to the modifications in the electronic properties of graphene. Thus, the large band gap opening around location A is mainly due to plastic regime marked by Stone Wall's defects. **Fig. 5(c)** reveals that the stress-strain behavior of graphene at location D (the trench slope) is purely elastic without any Stone Wale's 5-7-7-5 defects. However, as seen from **Fig. 5(d),** the different colors of these bonds represent the different relative bond lengths of graphene under the trench slope, displaying strongly asymmetric deformations in the form of six-membered rings. Interestingly, there were no plastic strains at location D (center of trench), yet a band gap opening of up to 0.87 eV was observed at this location due to asymmetric elastic straining. In **Fig. 5(e)**, the stress-strain behavior at location G is also elastic but relatively less as compared to location D. This relatively elastic deformation leads to more moderate asymmetric bond lengths in graphene six-membered ring (**Fig. 5(f)**), meaning the narrowest band gap opening. The evolutions of atomic structure at three locations A, D, G of strained graphene can also be revealed through molecular dynamics simulation, as show in Fig. S7-S9, dynamically verifying the different deformation process of atomic structure evolution in graphene under different strain. The description of the dynamic processes of molecular structure in at locations A, D and G, are demonstrated by MD simulation as shown in Supplementary Materials video 2.

We have closely followed experimental results on band gap opening DFT simulations, to estimate the band gaps in inhomogeneous straining graphene opened under different depth-to-diameter ratios, as shown in **Fig. 6**. The band gap values calculated by DFT vary based on location across the nanotrench depending on the level of straining. These values are often underestimated by DFT calculations as reported by previous researchers[9]. For the model of depth-to-diameter ratio of 100 nm/400 nm, the effective band gaps show a gradually decreasing trend from point A to G. It is interesting to note that band opening of up to 0.527 eV is observed at location G due to asymmetric strains in elastic regime, whereas band opening of ~1.365 eV is observed near the edge of the nanotrench (A point) due to dislocation-induced plasticity. The other two models of graphene (with depth-to-diameter ratios of 100 nm/300 nm and 100 nm/500 nm, details in Supplementary Materials, Fig. S12-13) are also investigated to indicate the higher strains in 3D inhomogeneous straining graphene with higher depth-to-diameter ratio, implying larger band gap opening under higher depth-

to-diameter ratio. The band gap opening is observed to be higher at the edge of the trench as compared to the center of the trench, attributing to the stronger sublattice asymmetry break of graphene at the edge of the trench. It is important to note that if the depth to diameter ratio is increased steeply (over 50%), then the graphene lattice at the edge of the trench could break and graphene would be converted to amorphous form.

Laser shock modulated inhomogeneous straining is thus an outstanding optomechanical technique with immense potential for applications, which would create semiconductor zones at the shallow slanted portions of strained graphene. The shape of graphene is at nanoscale from 30 nm to 200 nm, which can be controlled through precise design of the nanomold. A desired band gap can be provided by designing the mold dimension and applying appropriate laser shock pressure. This opens new possibilities for novel applications based on complicated nanostructures in 2D materials, such as topological insulators and quantum pseudo-magnetic field. Such freedom of designing the level of electronic band gap and the feasibility of selection of such high band gap zones at desired locations can also yield a new class of graphene-based metamaterials and can have a huge impact on future generations of optical and optoelectronic devices.

In summary, laser shock nanostraining of graphene on e-beam fabricated nanotrench-shaped nanomolds has been evaluated for electronic band gap engineering by scanning tunneling spectroscopy and other analytical techniques. For the first time, strain tunable band gap creation is observed in graphene with the band gap value up to 1.7~2.1 eV which attributes to asymmetric elastic-plastic straining behavior under the nanoscale ultrahigh strain rate imprinting process during laser shocking. Such a high level of band gap development in graphene without any extrinsic effects beyond graphene itself has not been reported earlier and is first of its kind. Numerous applications in electronics and optoelectronics based on such tunable band gap formation in graphene are enabled by this capability of converting the semi-metallic graphene to semiconducting graphene with designed band gaps.

Materials and methods

1. 3D straining of graphene:

CVD graphene coated on copper sheet was first transferred on SiO_2 mold by wet chemical transfer method. In brief, methylmethacrylate was coated (100 nm) onto graphene and then it was hardened to PMMA by heating the sample at 60 ^{0}C for 30 minutes. Copper was then etched away by using aqueous $FeCl_3$ solution. The copper-free sample was then gently transferred to clean deionized water and it was then transferred to fresh water for 3-4 times until there is no yellowish color remaining in water even after the sample is kept for 30 minutes. The graphene sheet having PMMA on the top was

then transferred to the SiO_2 mold while it was floating on the water surface. PMMA was then removed by dissolving it in acetone followed by isopropanol and deionized water respectively. The sample was then adequately dried in N_2 jet. The dried graphene was laser shock nanostrained by employing laser shock pressure on graphene sheet stretched on the SiO_2 mold. A pulsed (10 ns) Q-switch Nd:YAG laser (Continuum Surelite Ⅲ, Wavelength: 1064 nm) was used as an energy source for ablation. The laser beam diameter of 4 mm was attained by a focusing lens, which is calibrated by a photosensitive paper (Kodak Linagraph, type: 1895). Glass slide was used as the confining media, and aerosol graphite painting (Asbury Carbons, U.S.A.) was coated on thin (4 μm) aluminum foil (Lebow Company Inc., Bellevue, WA) as the ablative layer. Laser scanning was enabled by placing the sample on an X-Y-Z computer-controlled motorized stage. Silicon dioxide molds with nanofeatures were fabricated through electron beam lithography (EBL) or focused ion beam (FIB) milling and the trench width was 400 nm and 300 nm for the two trenches (Mold 1 and Mold 2). Depth was 100 nm for both mold trenches. To press the whole sample into the trenches, multiple laser pulses were implemented, the laser shocking location for each pulse was controlled by the X-Y-Z motorized stage.

2. Microscopy:

The surface morphology was imaged by an SEM (Hitachi S-4800 field-emission scanning electron microscope) at an operating voltage of 5 kV and an atomic force microscope (Veeco Dimension 3100 AFM) was employed to scan the nanoimprinted graphene surface at nanoscale under tapping mode.

3. STM, VS-STM and KPFM:

Omicron ultra-high vacuum (UHV) STM system was used to obtain the atomic resolved topographic image (I=10 nA, V=0.2 V). Scanning Tunneling Microscopy (STM) was then performed at room temperature Scanning Tunneling Microscopy (STM) was performed at room temperature in constant-current mode, with a set-point current between 200 and 350 pA and an applied sample bias between 2 and 3 V. The differential conductance, dI/dV, was measured using variable-separation scanning tunneling microscope (VS-STM), in which both the bias voltage and tip-sample separation are varied in a controlled manner. The *dI/dV* measurements were conducted at room temperature using a lock-in technique with a modulation voltage of frequency 1 kHz and amplitude 100 mV. A monolayer graphene is transferred onto the Al foil, followed by laser shock imprinting (LSI) process toward a 1600-nm periodicity trench mold. Kelvin probe force microscopy (KFPM) was used to characterize both topology and the distribution of contact potential difference (CPD) along the laser shocking imprinted area.

4. PL measurements:

Photoluminescence (PL) was measured by using Alpha 300R confocal Raman imaging system (WITec) at room temperature. The graphene was transferred onto the SiO2/Si nanomold, then Au electrode was deposited, followed by laser shock processing to compress the graphene into the nanonold. PL measurement was conducted before the electrical property testing (See Figure S4 inset for the structure of the device).

5. TEM:

The TEM samples for strained graphene were prepared by lift-out method by FEI Nova 200 focused ion beam (FIB) with a Klöcke nanomanipulator, to cut cross sectional view of the graphene vertical to the nanotrench. The top view of graphene near the edge of the nanotrench was also obtained for TEM by FIB. The microstructures are examined using a FEI Titan 80-300 and a Tecnal T20 transmission electron microscope (TEM).

6. Simulation:

Molecular dynamics simulations have been conducted to gain an insight of the deformation of the monolayer graphene and to understand the effect of the aspect ratio on the straining levels in graphene. Tight binding density functional theory has been employed to calculate the band structure of the strained graphene as a function of position for 3 molds with different aspect ratios. Work function at different seven locations on the strained graphene have also been calculated using DFT calculations. Details of calculation are described in the Supplementary Materials section.

Acknowledgements:

Financial assistance in the form of National Research Council Senior Research Associateship (G.J.C.), and NSF Grant Nos. CMMI-0547636 and CMMI 0928752 (G.J.C.) has been crucial for these experiments. National Natural Science Foundation of China (Grant No. 61704061). PK acknowledges financial support from Science and Engineering Research Board, Dept. of Sci. and Tech., Govt. of India in the form of The Ramanujan Fellowship (sanction no. SB/S2/RJN-205/2014).

Conflicts of interest

Authors declare no conflicts of interest.

References:

1. Novoselov, K. S. *et al.* Electric Field Effect in Atomically Thin Carbon Films, *Science* **306**, 666-669 (2004).
2. Novoselov, K. S. *et al*. Two-dimensional gas of massless Dirac fermions in graphene, *Nature* **438**, 197-200 (2005).
3. Geim, A. K., Novoselov, K. S. The rise of graphene, *Nature Mater.* **6**, 183-191 (2007).

4. Schwierz, F. Graphene transistors, *Nature Nanotech.* **5**, 487-496 (2010).
5. Bae, S. *et al*. Roll-to-roll production of 30-inch graphene films for transparent electrodes, *Nature Nanotech.* **5**, 574-578 (2010).
6. Han, T. H. *et al*. Extremely efficient flexible organic light-emitting diodes with modified graphene anode, *Nat. Photon.* **6**, 105-110 (2012).
7. Li, X. *et al*. Graphene-On-Silicon Schottky Junction Solar Cells, *Adv. Mater*. **22**, 2743-2748 (2010).
8. Schedin, F. *et al*. Detection of individual gas molecules adsorbed on graphene, *Nature Mater.* **6**, 652-655 (2007).
9. Robinson, J. T. *et al*. Reduced Graphene Oxide Molecular Sensors, *Nano Lett.* **8**, 3137-3140 (2008).
10. Lu, C. H. *et al*. A Graphene Platform for Sensing Biomolecules, *Angew. Chem.* **121**, 4879-4881 (2009).
11. Grigorenko, A. N., Polini, M., Novoselov, K. S. Graphene plasmonics, *Nat. Photon.* **6**, 749-758 (2012).
12. Chen, J. *et al*. Optical nano-imaging of gate-tunable graphene plasmons, *Nature*, **487**, 77-81 (2012).
13. Tielrooij, K. J. *et al*. Photoexcitation cascade and multiple hot-carrier generation in graphene, *Nature Phys.* **9**, 248-252 (2013).
14. Sun, D. *et al*. Ultrafast hot-carrier-dominated photocurrent in graphene, *Nature Nanotech.* **7**, 114-118 (2012).
15. Zeng, C. *et al*. Vertical Graphene-Base Hot-Electron Transistor, *Nano Lett.* **13**, 2370-2375 (2013).
16. Xia, F. *et al*. Ultrafast graphene photodetector, *Nature Nanotech.* **4**, 839-843 (2009).
17. Geim, A. K. Graphene: Status and Prospects, *Science* **324**, 1530-1534 (2009).
18. Novoselov, K. S. *et al*. A roadmap for graphene, *Nature* **490**, 192-200 (2012).
19. Lee, S. H. et al. Band Gap Opening by Two-Dimensional Manifestation of Peierls Instability in Graphene, *ACS Nano* **5**, 2964-2969 (2011).
20. Pereira V. M. & Castro Neto A. H. Strain Engineering of Graphene's Electronic Structure, *Phys. Rev. Lett.* **103**, 046801 (2009).
21. Jones G. W. & Pereira V. M. Designing electronic properties of two-dimensional crystals through optimization of deformations, *New J. Phys.* **16**, 093044 (2014).
22. Panchakarla, L. S. *et al*. Synthesis, Structure, and Properties of Boron- and Nitrogen-Doped Graphene, *Adv. Mater.* **21**, 4726-4730. (2009).

23. Guo, B. *et al*. Controllable N-Doping of Graphene, *Nano Lett*. **10**, 4975-4980 (2010).
24. Balog, R. *et al.* Bandgap opening in graphene induced by patterned hydrogen adsorption, *Nature Mater*. **9**, 315-319 (2010).
25. Kosynkin, D. V. *et al*. Longitudinal unzipping of carbon nanotubes to form graphene nanoribbons, *Nature* **458**, 872-876 (2009).
26. Kumar, P., Panchakarla, L. S. & Rao C. N. R. Laser-induced unzipping of carbon nanotubes to yield graphene nanoribbons, *Nanoscale* **3**, 2127-2129 (2011).
27. Zhou, S. Y., *et al*. Substrate-induced bandgap opening in epitaxial graphene, *Nature Mater.* **6**, 770-775 (2007).
28. Guinea, F., Katsnelson, M. I., & Geim, A. K. Energy gaps and a zero-field quantum Hall effectin graphene by strain engineering, *Nature Phys.* **6**, 30-33 (2010).
29. Ni, Z. H. *et al.* Uniaxial strain on graphene: Raman spectroscopy study and band-gap opening. *ACS nano* **11**, 2301-2305 (2008).
30. Mohiuddin, T. M. G. *et al*. Uniaxial strain in graphene by Raman spectroscopy: *G* peak splitting, Grüneisen parameters, and sample orientation, *Phys. Rev. B* **79**, 205433 (2009).
31. Rosenkranz, N. *et al*. Uniaxial strain in graphene and armchair graphene nanoribbons: an ab initio study. Annalen der Physik 523.1-2, 137-144 (2011)
32. Choi, S. M., Jhi, S. H., & Son Y. W. Effects of strain on electronic properties of graphene, *Phys. Rev. B* **81**, 081407R (2010).
33. Choi, S. M., Jhi, S. H., & Son Y. W. Controlling Energy Gap of Bilayer Graphene by Strain, *Nano Lett. **10***, 3486-3489 (2010).
34. Gui, G., Li, J., & Zhong, J. Band structure engineering of graphene by strain: First-principles calculations, *Phys. Rev B* **78**, 075435 (2008).
35. Cocco, G., Cadelano, E., & Colombo, L. Gap opening in graphene by shear strain, *Phys. Rev. B* **81**, 241412R (2010).
36. Hicks, J. *et al*. A wide-bandgap metal-semiconductor-metal nanostructure made entirely from graphene, *Nature Phys.* **9**, 49-53 (2013).
37. Ariza, M. P. *et al*. Stacking faults and partial dislocations in graphene, *Philos. Mag.* **92**, 2004-2021 (2012).
38. Yan, W. *et al*. Strain and curvature induced evolution of electronic band structures in twisted graphene bilayer,*Nat. Commun.* **4**, 2159-2164 (2013).
39. Levy, N. *et al*. Strain-Induced Pseudo–Magnetic Fields Greater Than 300 Tesla in Graphene Nanobubbles, *Science* **329**, 544-547 (2010).

40. Klimov, N. N. *et al*. Electromechanical Properties of Graphene Drumheads, *Science* **336**, 1557-1561 (2012).
41. Gao, H. *et al*. Large Scale Nanoshaping of Ultrasmooth 3D Crystalline Metallic Structures, ***Science*** 346, 1352-1356 (2014).
42. Zhang T., Gao H., Toughening Graphene with Topological Defects: A Perspective, J. Appl. Mechanics, **82**, 051001-1 (2015)
43. Wang X. *et al.* Enhanced rectification, transport property and photocurrent generation of multilayer $Rese_2/MoS_2$ p-n heterojunctions. *Nano Res.* **9**, 507-516 (2016).
44. Wei Z. *et al.* Molecular Heterojunctions of Oligo(phenylene ethylene)s with linear to cruciform framework. *Adv. Funct. Mater.* **25**, 1700-1708 (2015).
45. Wang Q. H. *et al.* Electronics and optoelectronics of two-dimensional transition metal dichalcogenides. *Nat. Nanotechnol.* **7**, 699-712 (2012).
46. Ye L. *et al.* Highly polarization sensitive infrared photodetector based on black phosphorus-on-WSe_2 photogate vertical heterostructure. *Nano Energy* **37**, 53-60 (2017).
47. Mott, P. H., A. S. Argon, and U. W. Suter. "Atomistic modelling of plastic deformation of glassy polymers." Philosophical Magazine A 67.4 (1993): 931-978.
48. Stukowski, Alexander, and A. Arsenlis. "On the elastic–plastic decomposition of crystal deformation at the atomic scale." Modelling and Simulation in Materials Science and Engineering 20.3 (2012): 035012.

Figure Captions:

Fig. 1 (a) Schematic diagram illustrating experimental setup of laser shock, the inset is the depiction of nano-shaped graphene along with schematic representation of graphene's band opening due to aymmetric elastic straining and plastic straining, under elastic strain, the lattice preserves the six-atom ring structure, but under plastic strain, five and seven atom ring are emerging. (b) Evolution of nanoshaped graphene under laser shock, (c) FESEM image of SiO_2 mold used for the purpose, (d)-(e) show zoomed in version. (f) Nanotrenches with depth 100 nm. (g) AFM images of shaped graphene with mold 1 (400 nm in width and 100 nm in depth), and (h) is the zoomed AFM profile (i) Raman spectra mapping of unstrained graphene and strained graphene in the nanotrench.

Fig.2 (a) Schematic of the STM measurement on nanoimprinted graphene sheet. (b) The calculated strain as a function of position along the trench using MD simulations, the inset shows the details of locations of band gap measurements by STM (room temperature in constant-current mode, with I_{setp}= 0.2nA and V_{bias}= 2V). (c) The representative (*dI/dV*)/*I-V* measurements on the patterned graphene sheet at various locations from point 1 to point 7, as shown in the inset of (b). (d) Scanning tunneling microscopy image of graphene strained on the same nano-trench and (e) the corresponding effective band gaps as a function of position along the white dashed line in (d). (f) Profiles for topology and CPD (g) Atomic force microscopy (AFM) 3D surface profile of topology of graphene on silicon mold and (h) is the corresponding KPFM image (i) DFT calculated and measured results of work function for the strained graphene at various locations along the trench.

Fig. 3 Large scale patterned graphene sheet. (a) STM mapping and (b) SEM image of the patterned graphene. The inset in (a) shows the FFT results, which indicates the periodicity of patterned graphene. (c)-(i) The STM current measured at several locations on the yellow line on (a), which indicates the periodic modulation of graphene's band gap.

Fig. 4 (a) TEM image (b) HRTEM image of selected region shown in (a); (c) atomic spacing in (b). (c) TEM image of another region of strained graphene (e) HRTEM of the region shown in (c). Distances along three directions are shown in (e). Omicron (UHV) STM system was used to obtain the atomic resolved topographic image (I=10 nA, V=0.2Volt) and study the effect of laser shock straining on the atomic movements and reconfigurations. (f), (g) and (h) STM images of strained graphene sheet at three different locations, from the trench valley, the slope of trench, and the trench edge, respectively. The atomic crystal structure is marked by light blue lines.

Fig. 5 (a) Depicts the stress-strain response extracted at the edge of the nano-shaped graphene. It is clear from the plot that graphene undergoes through elasto-plastic deformation which is also depicted by the 5-7-7-5 defects seen from figure (b). Ratios of bond lengths were calculated and plotted as seen in figure (b) where green marks the average bond length of pristine graphene 1.42 Å. Fig (c) and Fig (e) depict the elastic stress -strain response at location D and location G of deformed graphene and (d) and (e) denote bond length ratio. It is interesting to note that band gap opening of 0.527 eV was observed at this location due to asymmetric strains because of asymmetric bond length ratios even in elastic regime.

Fig. 6 Band structure for strained graphene at different locations marked (a) to (g) from edge to center were plotted. The band gap opening at regions near the edge were found out due to onset of plasticity and the band gap opening near the center was found out due to asymmetric elastic straining in graphene. Fig (h) depicts the band gaps at different locations from edge to center for all three configurations with diameters of 300 nm (Aspect Ratio: 33%), 400 nm (Aspect Ratio: 25%) and 500 nm (Aspect Ratio: 20%). Higher band gap opening is observed at lower aspect ratios near edge of strained graphene.

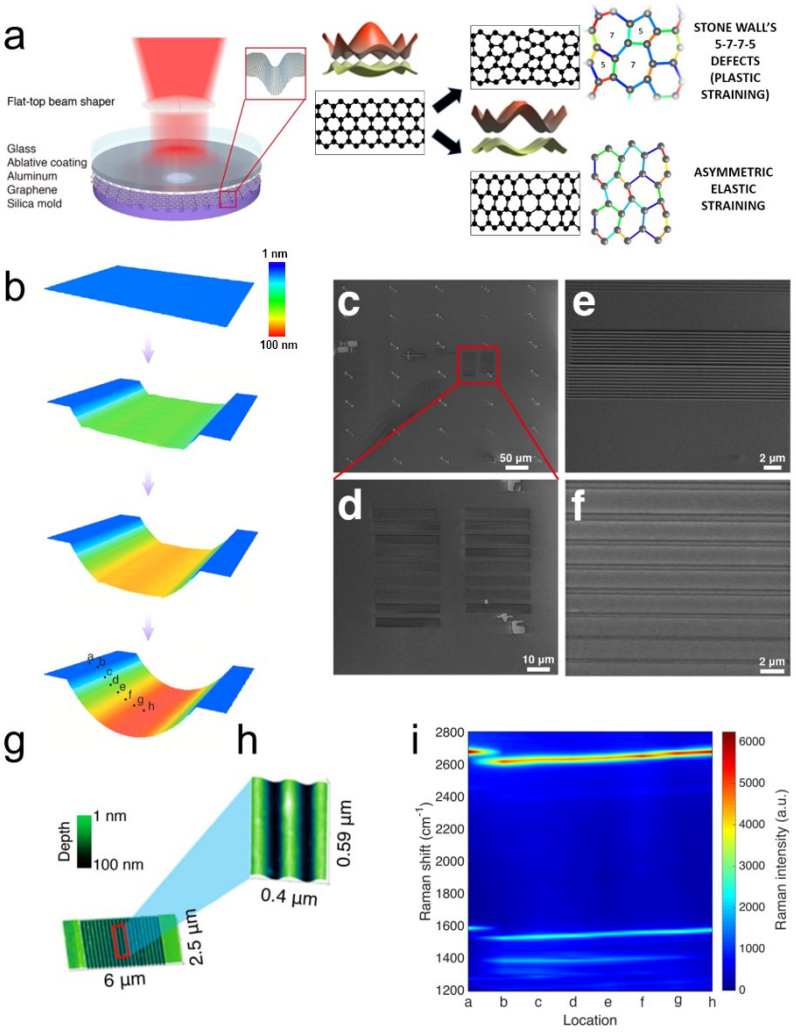

Fig. 1

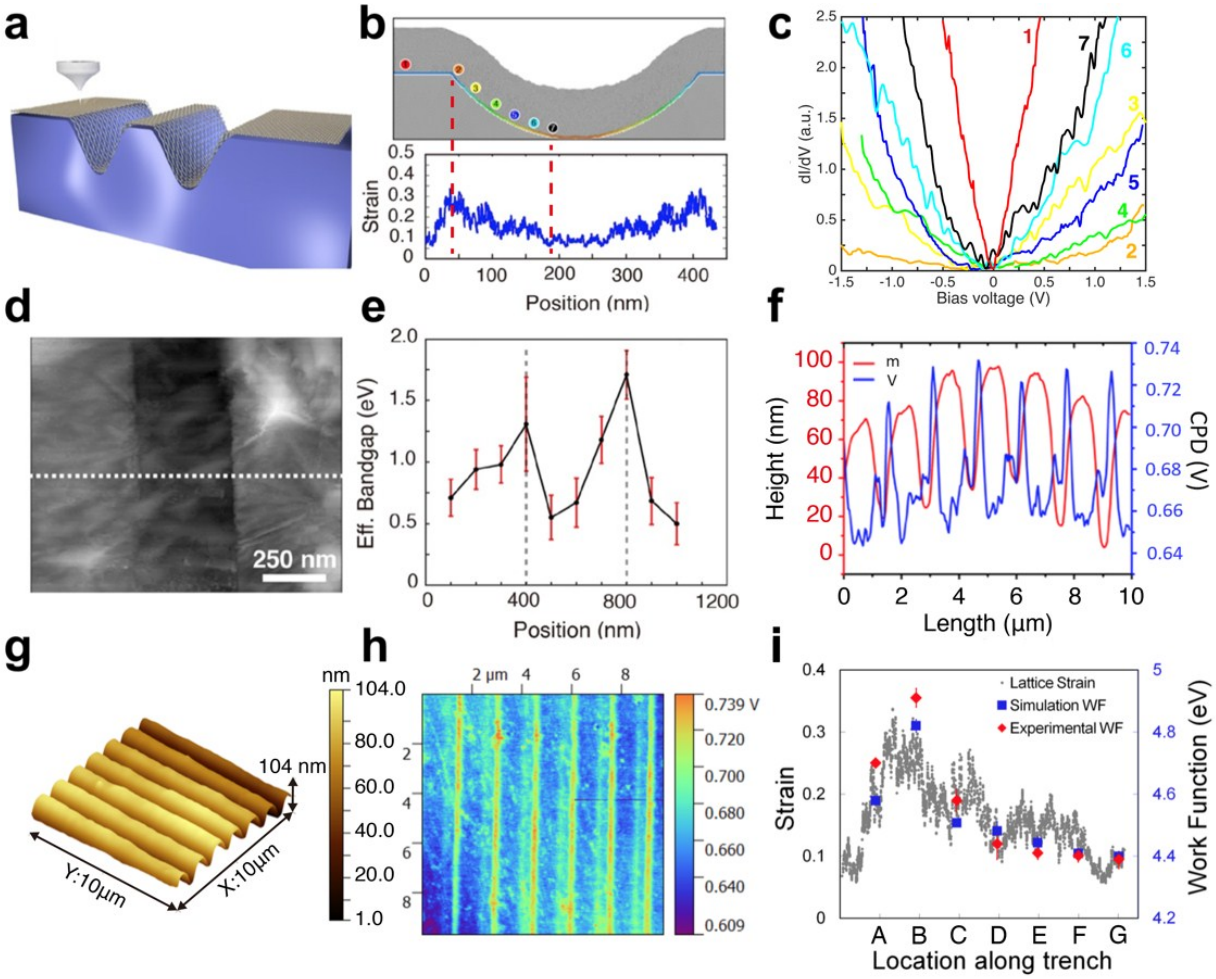

Fig. 2

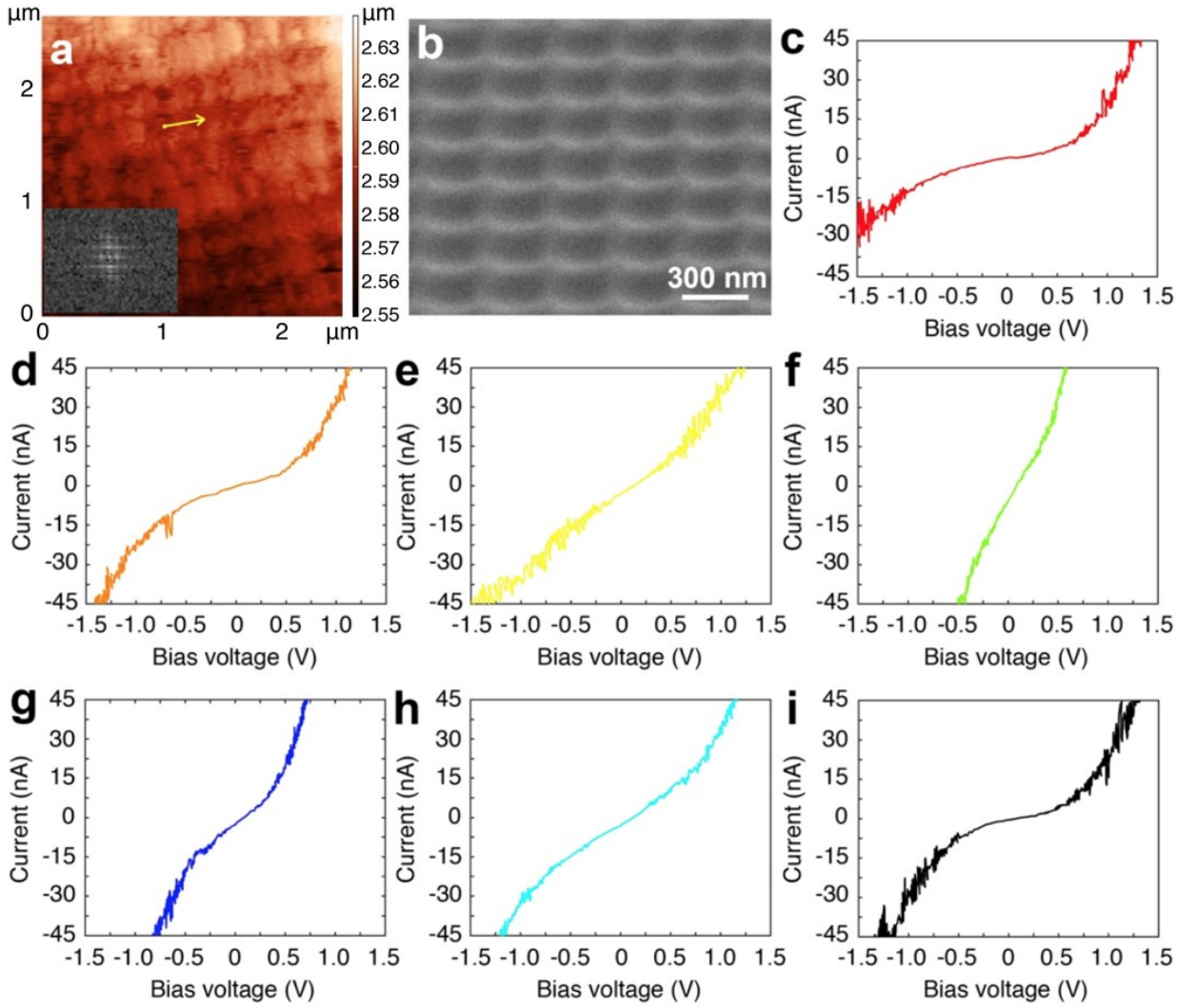

Fig. 3

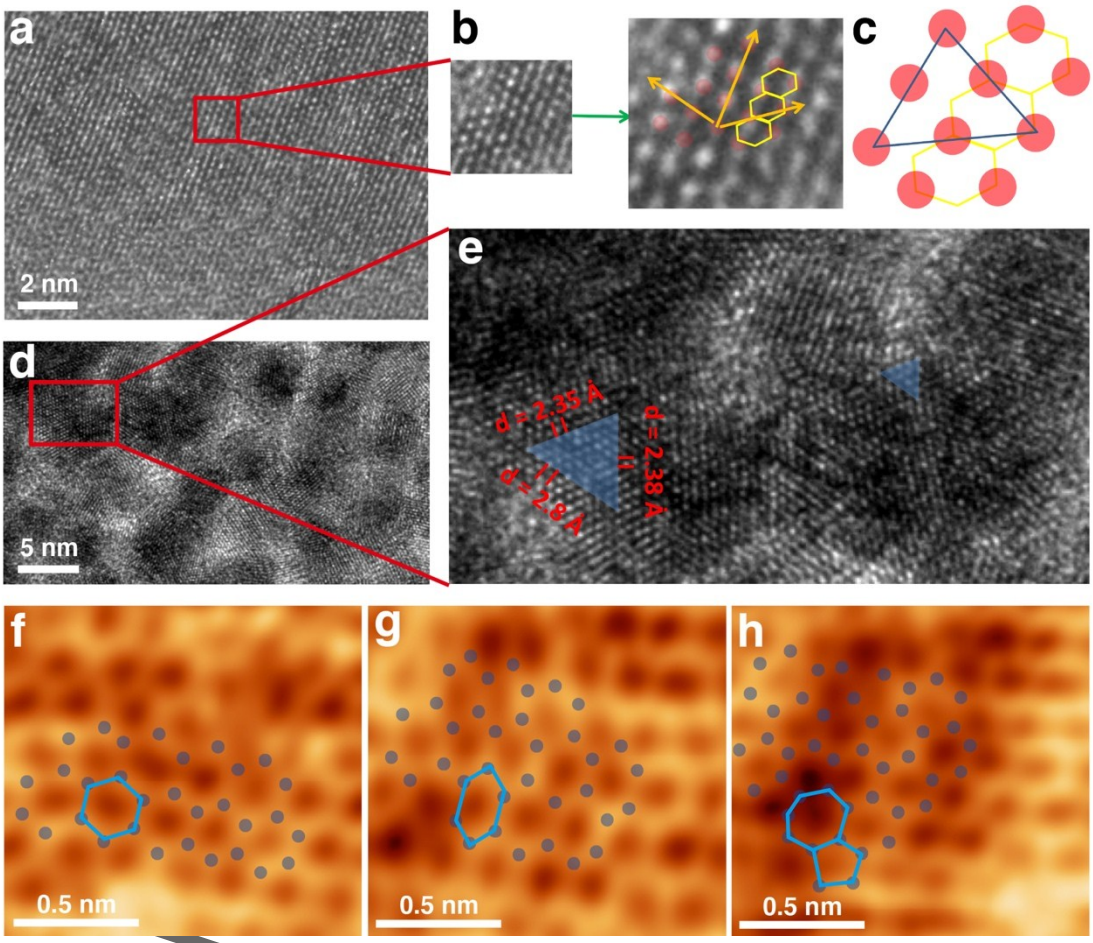

Fig. 4

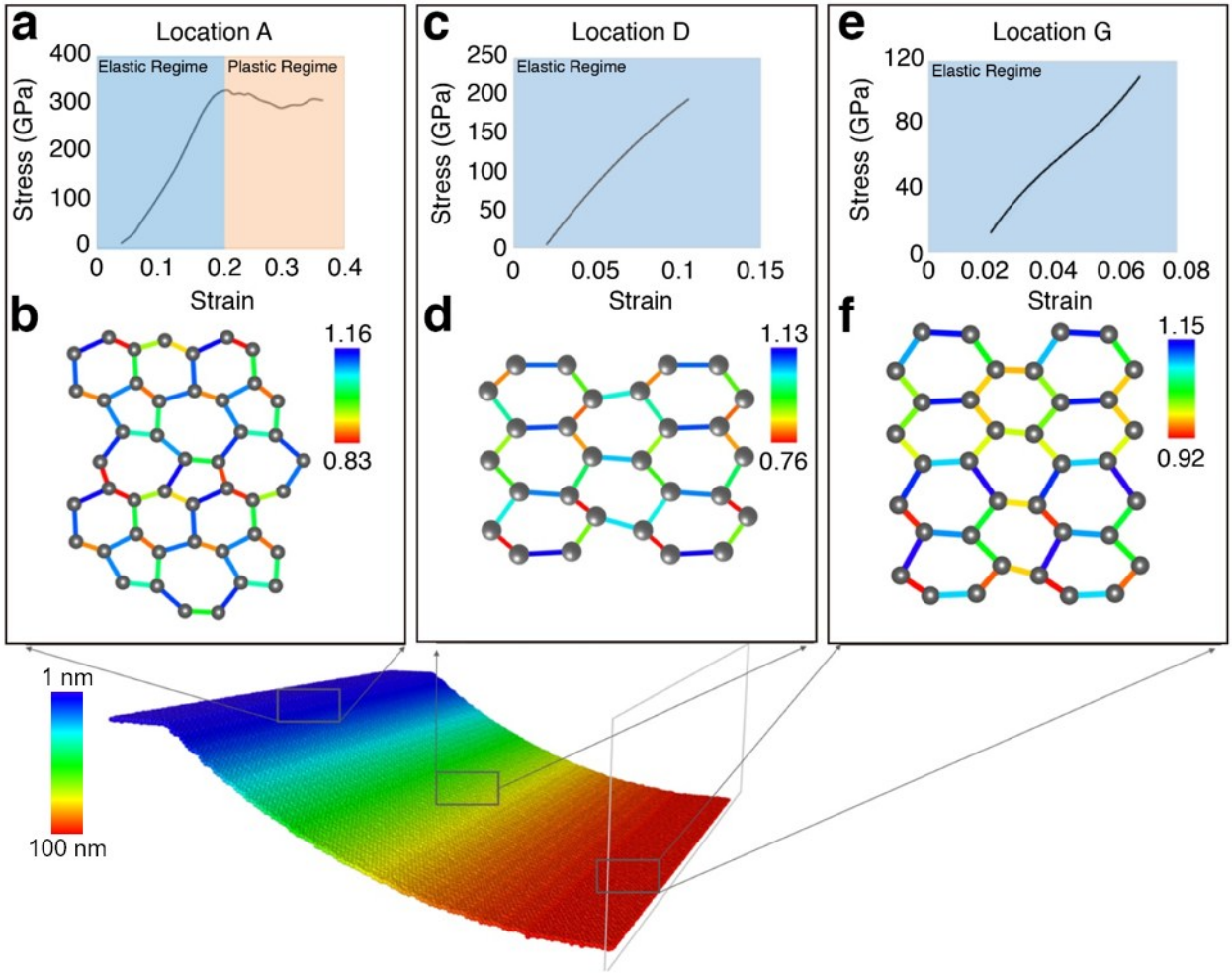

Fig. 5

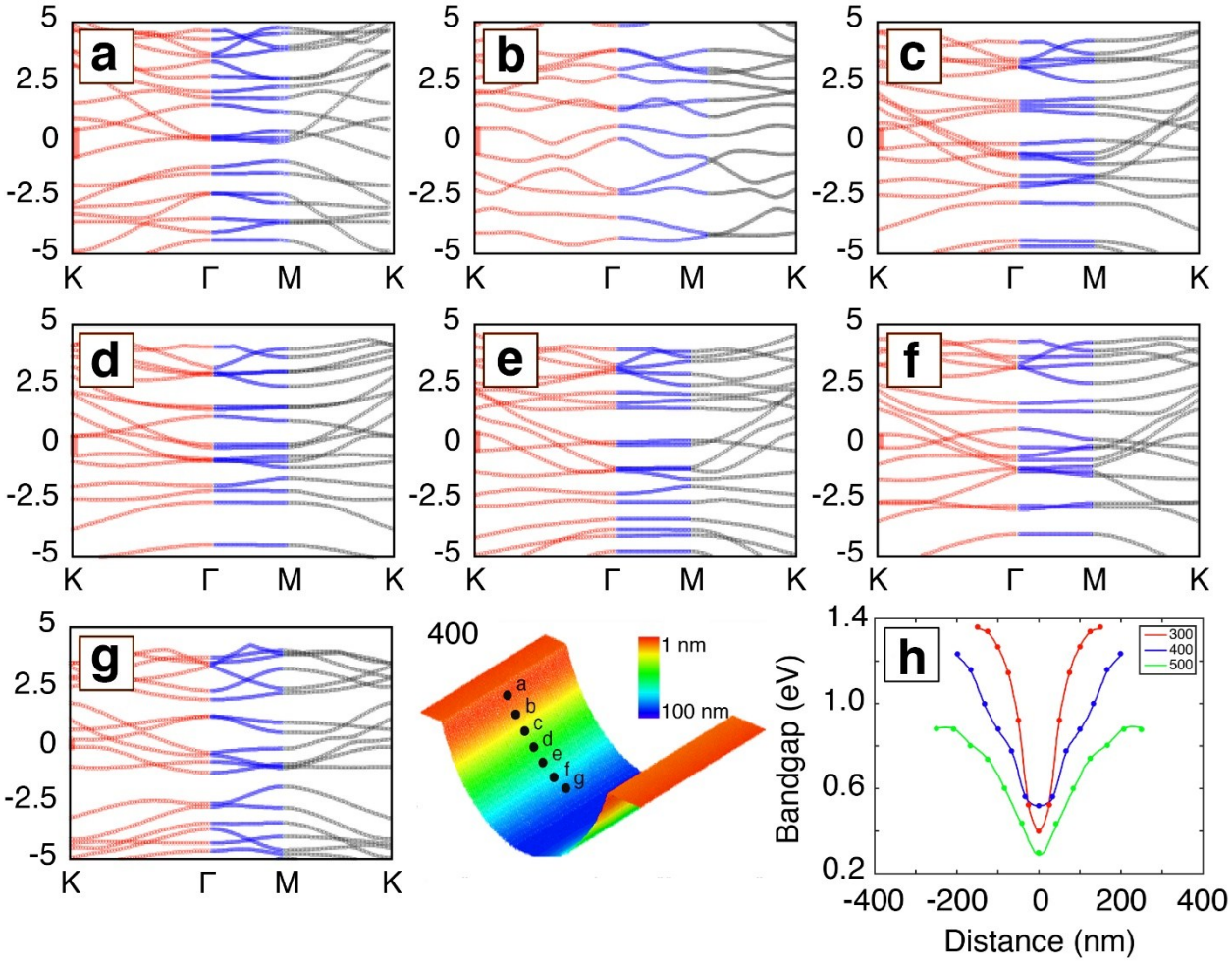

Fig. 6

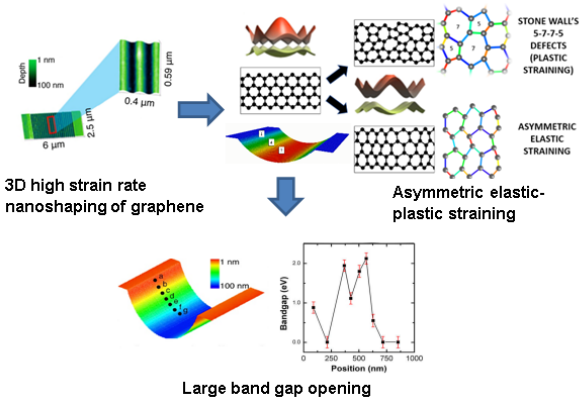

Our work demonstrates an easy and effective opto-mechanical way to modulate both the band gap structure and the Fermi-level of monolayer graphene. The laser shock induced 3D nano-shaping enables an asymmetric elastic - plastic straining of graphene, resulting in a wide graphene band gap over 2.1 eV and a wide Femi-level adjustment range of 0.6 eV.